Crystal Delay and Time Walk Correction Methods for Coincidence Resolving Time Improvements of a Digital-Silicon-Photomultiplier-Based PET/MRI Insert

David Schug, Bjoern Weissler, Pierre Gebhardt, and Volkmar Schulz

Abstract—**Our group has built the MRI compatible PET insert Hyperion II^{D}, which is based on digital silicon photomultipliers [digital photon counters (DPCs)]. We characterized its performance for two different scintillator configurations already in previous publications. For this paper, we reused the raw detector data that were used in previous publications and stored for offline analysis. We reprocessed these data in order to improve the timing performance of the PET scanner. Different crystal delay and time walk calibration and correction methods are evaluated with respect to the coincidence resolving time (CRT) of the scanner. For all applied correction methods, we report CRTs both for a preclinical and a clinical scintillator configuration for all DPC trigger schemes and several energy windows. The newly obtained results were compared with the previously published values, and the additional benefit of using a time walk correction was evaluated. Previously published CRTs could be improved using a refined version of the original crystal delay calibration method without applying a walk correction by 6.3%–10.9% for a wide energy window ranging from 250–625 keV, and we could show an additional improvement of up to 2.6% by adding a walk correction. Using trigger scheme 1 and a very narrow energy window around the photopeak (500–520 keV), we could reach CRT values on system level of 208/240 ps for the clinical/preclinical scintillator configuration.**

Index Terms—**Instrumentation and measurement/Scintillation counters, magnetic resonance imaging, photodiodes. positron emission tomography, scintillators, semiconductor detectors.**

I. INTRODUCTION

OUR group has built the Hyperion II^{D} PET insert, which aims at preclinical imaging and can be inserted into and operated simultaneously with a standard clinical 3-T MRI scanner (Philips Achieva) [1]–[3]. It employs digital silicon photomultipliers (dSiPMs) [4] to detect the optical light emitted by pixelated LYSO scintillators. Two different scintillator geometries have been used to equip full imaging-capable systems for which a calibration and a performance evaluation were conducted [5], [6].

In PET, the two gamma photons are measured and need to be correlated to determine if both were emitted from the same positron annihilation [7]. Due to the back-to-back emission of the two gamma photons, the location of the positron annihilation can be constrained to the line of response (LOR) connecting the two gamma–detector interactions. If the time difference between the two gamma interactions can be determined with very high resolution, in the order of a few hundreds of picoseconds, the location of the annihilation along the LOR can be determined. The spatial resolution along the LOR is directly proportional to the ability of the PET system to resolve the time difference. This method is called time-of-flight PET and can be used to increase the signal-to-noise ratio of the PET image [8].

This so-called coincidence processing of the two signals caused by the two gamma interactions can either be realized by analog signal processing [9] or, as done in modern scanners [10], by assigning time stamps to each gamma detection and then correlate them in a central coincidence unit. This can be implemented as a dedicated electronic circuit, in firmware of a field-programmable gate array (FPGA) or in software [11]. For the approach using local timestamps, precise and globally valid timing information is needed for each of the gamma–crystal interactions. Our PET scanner uses a global reference clock that is distributed to all photosensors of the system.

The centrally generated clock signal may be changed by the routing through signal cables and traces and all the components used for the clock distribution. Delays are introduced by the signal run time in cables, printed circuit board traces, and signal routing paths in the firmware of the used FPGAs. Electronic components used for the signal distribution or conversion from electrical to optical signals and vice versa are also potential sources of signal delays. Furthermore, all these components may introduce a jitter to the clock signal. A fixed delay, which is accounted for, will not deteriorate the timing resolution of a PET system. Whereas jitter, on the other hand, will add statistical uncertainty to the clock signal and directly affects the timing resolution of PET a system.

Manuscript received August 14, 2016; revised December 14, 2016; accepted January 13, 2017. Date of publication January 26, 2017; date of current version March 24, 2017. This work was supported in part by the European Community Seventh Framework Program "SUB Nanosecond Leverage in PET/MR Imaging" under Project 241711, in part by Philips Research Europe, Aachen, Germany, and in part by the European Union's Horizon 2020 research and innovation program under Grant 667211.

D. Schug, B. Weissler, and P. Gebhardt are with the Department of Physics of Molecular Imaging Systems, Institute for Experimental Molecular Imaging, RWTH Aachen University, 52074 Aachen, Germany.

V. Schulz is with the Department of Physics of Molecular Imaging Systems, Institute for Experimental Molecular Imaging, RWTH Aachen University, 52074 Aachen, Germany, and also with the Department of Molecular Imaging Systems, Philips Research, 52074 Aachen, Germany.

Color versions of one or more of the figures in this paper are available online at http://ieeexplore.ieee.org.

Digital Object Identifier 10.1109/TNS.2017.2654920

Besides the clock signal distribution, the physical gamma detection process is a further source of time delay and jitter. The time stamp of a gamma interaction is generated when the photosensor detects the optical scintillation light. The optical photons are generated in a statistical process, which can be modeled as an exponential distribution with a certain time constant, which is a property of the scintillator material. These optical photons then have to travel to the sensitive area of the photosensor and are detected with a certain probability. Upon detecting the required number of photons the photosensor will generate a trigger, which is then assigned a time stamp based on the provided clock signal. This introduces a fixed mean delay depending on the mean time it takes for the required number of optical photons to travel from the location of the scintillation to the photosensor and being detected by it. This mean delay is not only dependent on the location of the gamma interaction in the scintillator but also on the amount of optical photons that are produced and thus on the deposited energy in the scintillator. Gamma interactions at the exact same location in the scintillator will show different mean delay values depending on the energy deposited by the gamma as they will result in a different mean number of optical photons produced. More photons will lead to an earlier time stamp generation as the required number of detected photons will be reached earlier. This is the so-called time walk effect [12, chapter 17], which can also be modeled to improve the overall timing performance of the PET system. In addition to a mean delay, the statistical process of optical photon generation, transport, and detection introduces a jitter, which will deteriorate the achievable timing resolution of a PET system.

If delays (either due to clock signal distribution or due to effects of the optical-photon-detection process) are present in a PET system and are not corrected for, the coincidence processing needed for the correlation of two gamma interaction will suffer from a nonoptimal coincidence resolving time (CRT). The same is true if the time walk effect is not corrected for. If both effects are addressed properly, the CRT of the PET system is dominated by the jitter of the clock signal distribution and the jitter of the generation, transport, and detection process of optical photons.

For the timing calibration, we employed several point sources at known locations in the scanner's field of view (FOV). The locations can be reconstructed with high precision with the PET, and no mechanical reference has to be provided. The positron-emitting sources were used to determine the photsensor delay values as well as additional delays caused by the location of the crystal scintillator element with respect to the photosensors (details about these calibration steps are given in Section III).

Besides the delay calibration, we also performed a time walk calibration using the same data.

In this paper, we revisited the timing calibration applied to two different PET systems in order to improve the CRT performance. In the previously published works, we calibrated only fixed time delays for sensors and crystals [13] and did not correct for the time walk effect. Nonetheless, we could achieve CRT values of 215.2 ps full-width at half-maximum (FWHM) for the most favorable combination of parameters with regard to the timing performance tested using a *clinical* scintillator configuration [6]. The goal of this paper is to reprocess previously acquired raw detector data and present results of different existing time delay and time walk calibration and correction methods and show the improvements compared with the previously published results.

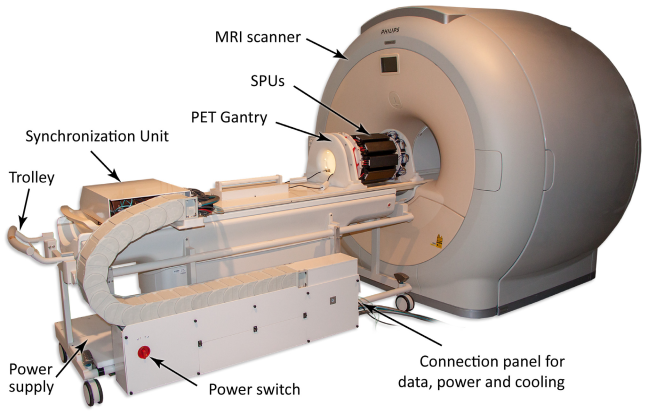

Fig. 1. Gantry of the PET insert holds ten SPUs. The gantry is mounted on a trolley, which allows easy insertion into the clinical MRI scanner. A synchronization unit and a power supply are also mounted onto the trolley. Only a single data cable, a power cable, and the cooling tubes have to be connected, which allows for an easy installation and mobile setup (adapted and reprinted from [1] 🅭🅯3.0).

II. MATERIALS

The Hyperion II^{D} PET/MRI insert (Fig. 1) is designed to fit into a clinical MRI and thus provides simultaneous PET/MRI image acquisition. A good overview about the hardware architecture is given in [1]. We employ LYSO scintillators, which are read out by a sensor tile, which is 32.6 mm $\times$ 32.6 mm in size and made up of 16 dSiPMs that are also called digital photon counters (DPCs) (Philips Digital Photon Counting DPC3200-22) [14]–[17]. Up to six of these sensor tiles can be mounted via interface boards, equipped with an FPGA for the readout of the DPCs [18], on a singles-processing unit (SPU) [19] in a 2 $\times$ 3 arrangement [Fig. 4(b)]. Ten of these SPUs are mounted on a gantry to form the PET ring with a maximum axial FOV of the sensor area of 99.2 mm and a sensor-to-sensor distance in transaxial direction of 237.6 mm. A liquid cooling circuit is located in between the sensor tile and the interface board, and is hooked up to a process thermostat, which allows us to operate the DPCs at a controlled temperature.

The SPUs are connected to a data acquisition and processing server [11], [20], which is able to store the complete raw DPC data stream on hard disks for later offline analysis. This unique feature allows the user to implement a calibration and processing framework in software and to reprocess the same measurement with different algorithms.

So far, two different scintillator geometries were used. The *preclinical* configuration uses a pixelated LYSO scintillator array with a height of 12 mm and a pitch of 1 mm coupled to the DPC array via a 2-mm-thick light guide [5], [13] [sketch in Fig. 2(a) and photo in Fig. 3]. In this configuration,

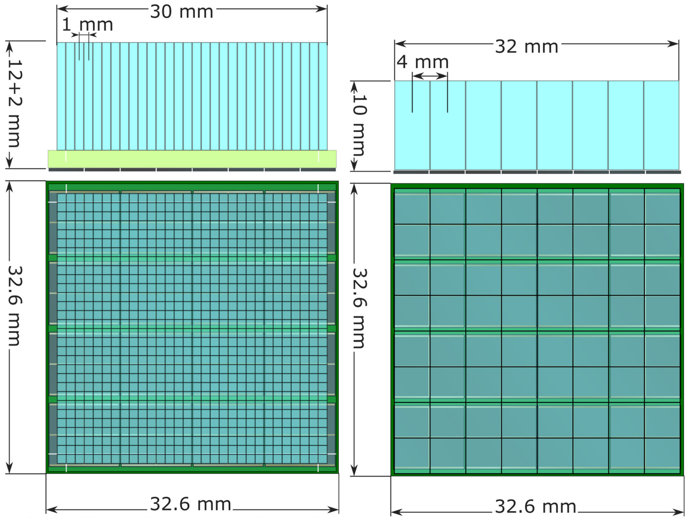

(a) preclinical detector configuration (b) clinical detector configuration

Fig. 2. Sketches of the detector stack configurations. (a) *Preclinical* detector configuration employs a light guide between the LYSO scintillator and the sensor tile. (b) *Clinical* detector configuration used in this paper uses a one-to-one coupling of crystals to readout channels. The sensitive pixels of the DPCs are drawn in dark gray. The horizontal areas between DPCs drawn in light green are the bond gaps that are insensitive (reprinted from [6] 🅭🅯3.0).

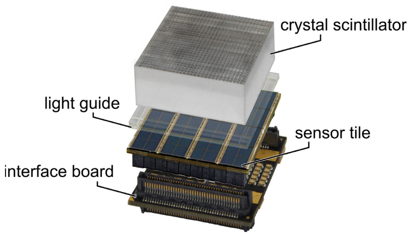

Fig. 3. Exploded-view photo of the detector stack of the *preclinical* configuration. (The reflective film on top of the crystal array has been removed to show the individual crystals.) In the final scanner, after the components have been glued together, the detector stack is wrapped with Teflon tape to close up the optically transparent light guide (adapted and reprinted from [13] 🅭🅯3.0).

the SPUs are fully equipped with six detector stacks. The *clinical* scintillator configuration uses a one-to-one coupling scheme of LYSO crystals to readout channels (10-mm height and 4-mm pitch) [6], [21] [sketch in Fig. 2(b) and photo in Fig. 4(a)] and only two of the six possible detector stacks resulting in one fully equipped PET ring instead of three [Fig. 4(b)]. All crystals are wrapped in 67-μm Vikuity$^{\text{TM}}$ ESR film (3M, St. Paul, USA).

We used five point-like ^{22}Na sources with an active diameter of 0.25 mm and an activity of 1.1–1.5 MBq each enclosed in a cast acrylic cube with an edge length of 10 mm (NEMA cubes) for the time calibration and the CRT-related investigations.

A. DPC3200-22 Details and Trigger Network

The DPC3200-22 is made up of four channels (also called pixels), each consisting of 3200 single-photon avalanche diodes (SPADs) and a global time-to-digital converter (TDC) shared by the four pixels. Each pixel is, in turn, split up in four so-called subpixels [see Fig. 5(a)] which generate a subpixel trigger signal on the event of a breakdown of one of the 800 SPADs. To generate the pixel trigger signal and to determine the timestamp, the four subpixels of a pixel can be connected logically using different trigger schemes [see Fig. 5(b)]. These trigger schemes, the corresponding logical combinations of subpixel trigger signals, and the resulting mean number of randomly distributed SPAD breakdowns on a pixel are listed in Table I. The four pixel trigger signals are all connected by a logical OR to the TDC (for more details, see [23]). The DPC promises to deliver excellent timing performance, especially when using the lowest trigger threshold [24]. In order to reduce the overall dark count rate, i.e., the number of noise-induced triggers per time interval, SPADs can be deactivated individually [14].

TABLE I

DPC3200-22 TRIGGER SCHEMES AND THE RESULTING THRESHOLDS IN SPAD BREAKDOWNS PER PIXEL

Trigger Scheme	Sub-Pixel (sp) Configuration	Average Threshold / SPAD breakdowns
1	sp1 $\vee$ sp2 $\vee$ sp3 $\vee$ sp4	1.00 ± 0.00
2	[(sp1 $\vee$ sp2) $\wedge$ (sp3 $\vee$ sp4)] $\vee$ [(sp1 $\vee$ sp4) $\wedge$ (sp2 $\vee$ sp3)]	2.33 ± 0.67
3	(sp1 $\vee$ sp2) $\wedge$ (sp3 $\vee$ sp4)	3.00 ± 1.40
4	sp1 $\wedge$ sp2 $\wedge$ sp3 $\wedge$ sp4	8.33 ± 3.80

III. METHODS

In the following, first, the used data sets are described, and then the data processing to calculate the gamma photon's location, energy, and time stamp from DPC raw data is sketched. Next, the energy windows used in this paper are defined followed by an explanation of how the system CRT is calculated from detected and accepted coincidences. In Section III-E, a general explanation of the timing calibration is given and the difference between a calibration method based on individual crystal pairs and a one-to-many coupling approach is explained. Section III-F describes how the DPC sensor delays are determined. The next section describes several different methods on how to determine the additional constant crystal delay values. Section III-H explains the methods used to calibrate and correct for the energy-dependent time walk effect. Section III-I reports the combinations of time delay and time walk corrections that are evaluated in this paper.

A. Used Data Sets

In this paper, we used the raw DPC data of original and already published measurements obtained with the Hyperion II$^{\text{D}}$ platform. For the *preclinical* configuration, we used data obtained with an overvoltage of $V_{\text{OV}} = 2.5$ V at a cooling-liquid temperature of -5 °C (operating temperatures between 3.17 ± 1.15 °C and 4.48 ± 1.45 °C), a validation threshold of 16.9 ± 6.2 photons, and a validation length of 40 ns. The positions and activities of the five point sources are given in Table II. These raw data were already used for publication [5, Table S1] (constant V_{bias} with IDs 1, 7, 19, and 21).

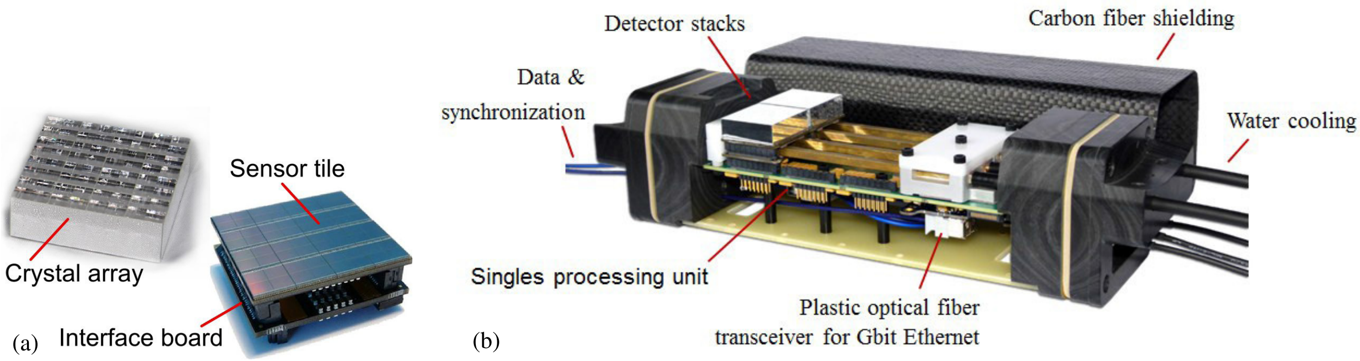

Fig. 4. (a) Detector stack consists of an interface board, the sensor tile, and a crystal array (from the *clinical* configuration). (b) SPU is equipped with two detector stacks (reprinted from [22], © 2012 IEEE).

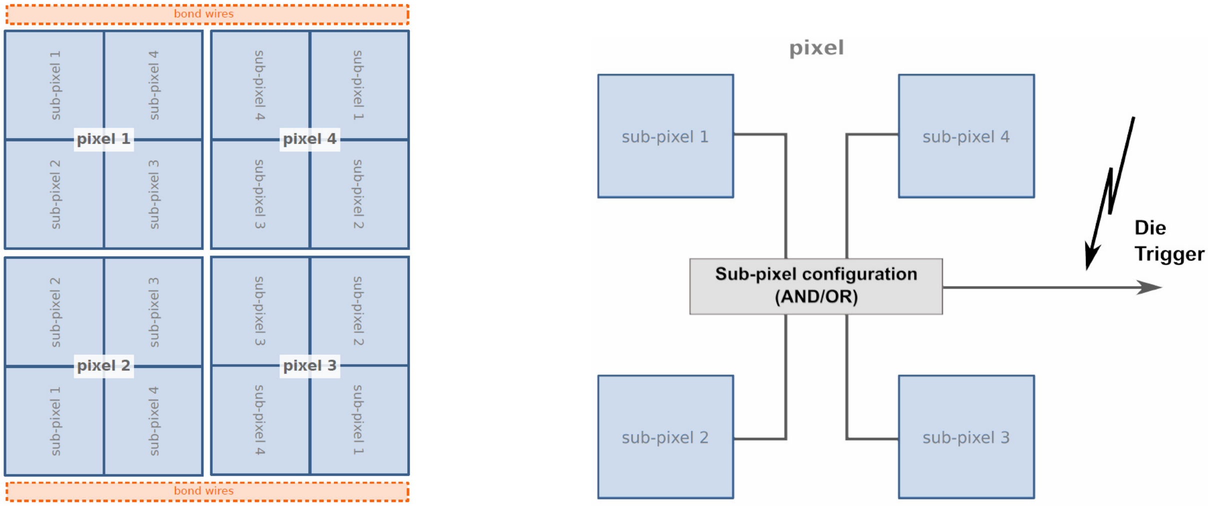

(a) DPC3200-22 division in sub-pixels

(b) DPC3200-22 sub-pixel trigger logic

Fig. 5. (a) Sketch of a DPC3200-22. Each of the four pixels is subdivided into four subpixels. The DPC3200-22 outputs the number of broken down SPADs per pixel. (b) Trigger generation logic. The trigger signals of each subpixel of one pixel can be connected with four different logical operations to generate the pixel trigger signal (see Table I). The trigger signals of the four pixels are connected by a logical OR to the TDC (both reprinted from Philips Digital Photon Counting [25], courtesy of PDPC).

TABLE II

SOURCE POSITIONS OF THE FIVE NEMA CUBES USED FOR THE MEASUREMENTS WITH THE *Preclinical* CONFIGURATION ($x = y = z = 0$ IS THE CENTER OF THE SCANNER) (REPRINTED FROM [5] CC BY 3.0)

NEMA cube	x/mm	y/mm	z/mm	activity/MBq
1	-0.6	-1.8	-0.5	1.48
2	-1.3	-1.7	30.2	1.37
3	-0.6	-1.8	-15.5	1.28
4	-1.5	-1.7	14.4	1.25
5	-0.2	-1.8	-32.1	1.20

For the *clinical* configuration, we used measurements obtained with an overvoltage of $V_{\mathrm{OV}} = 2.5$ V at a cooling-liquid temperature of -5 °C (operating temperatures between 0 °C and 5 °C), a validation threshold of 52 photons, and a validation length of 5 ns. Again, the five ^{22}Na point-like sources were used with a combined activity of 5.53 MBq and were distributed centrally along the axial axis with positions at: $(x, y, z) \approx \{(-11.9, -3.1, -9.2), (-0.7, -10.4, -8.1), (-2.0, -4.2, 0.0), (9.0, -6.7, 5.1), (-3.2, 1.6, 9.5)\}$ mm (here, $z = 0$ is the middle of the single PET ring). These raw data were already used for a publication [6] (PET-only measurements of five point sources).

As usual, 20% of the noisiest SPADs per pixel were deactivated.

B. Processing From Raw Data to Singles and Coincidences

DPC raw data of the *preclinical* configuration [Fig. 2(a)] were clustered using a time window of 40 ns and processed to singles using a center-of-gravity algorithm as described in [13]. For the *clinical* configuration [Fig. 2(b)], a cluster window of 5 ns and a direct crystal identification as described in [6] including an inter-crystal scatter rejection filter were used. Throughout this paper, we employed a time window of 3 ns to check for coincidences and only accepted coincidences with a maximum distance of 10 mm to the closest point source.

After having calibrated the sensor delays of the system (described in detail in Section III-F) and applied the original

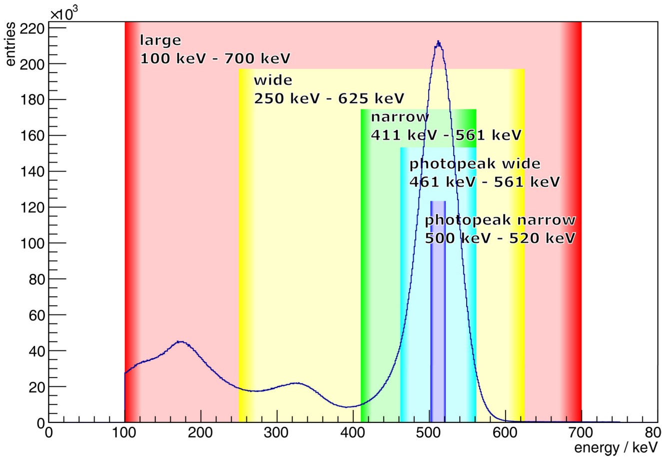

Fig. 6. Coincident energy spectrum obtained with the *clinical* configuration and trigger scheme 4. The energy windows used in this paper are marked in color. The different heights of the energy ranges are used only for better distinction and placement for the labels.

crystal delay calibration method (details in Section III-G1) to the raw data, the latter was processed to obtain singles and coincidences using a very large energy window of 100–750 keV and stored as a listmode file containing timestamps and energy values for each single. This listmode file was then used for all further calibrations and evaluations without the need to reprocess the raw data. All further time stamp corrections (delay and/or time walk) were applied to the time stamp of the singles, which are stored in the listmode file individually.

C. Reference Energy Window and Evaluation Energy Windows

The reference energy window in this paper was set to 411–561 keV and was used to determine calibration values of the various methods (detailed descriptions of the methods are given in the following sections). The calibration values for crystal delay and time walk were determined using the reference energy window. Based on that, the CRT is reported for a variety of energy windows with the same calibration values. The CRT is reported for the energy windows that are graphically represented in Fig. 6.

D. CRT Calculation

The CRT is determined from the system time difference histogram containing all accepted coincidences with their time difference corrected for the closest source position. LORs with a distance greater than 10 mm to the closest source position are discarded based on the signal window used for the sensitivity evaluation of the preclinical NEMA NU 4-2008 standard. Analogous to our previous publications, the CRT FWHM was determined by fitting a Gaussian to the central part of the spectrum. The fit range was chosen as -0.5 FWHM to 0.5 FWHM around the peak. No background modeling or removal was applied, and the FWHM used for the fit range was determined by applying an initial preliminary fit. The FWTM was determined with an exponential function fitted to the spectrum in a range $\pm 25\%$ around the location of the FWTM for each side. This fit was performed iteratively to center the FWTM location close to the middle of the fit range (difference smaller than 10%). Based on the result of the Gaussian fit of the central part of the spectrum, the expected FWTM assuming a fully Gaussian distribution can be calculated ($\text{FWTM} \approx \text{FWHM}/2.355 \cdot 4.294$). Any additional excess of the FWTM determined with the previously described fitting method can be seen as a measure of the tail component of the time difference spectrum. We report in this paper the relative additional width of the calculated FWTM compared with the expected Gaussian FWTM from the central part (the abbreviation used for the Gaussian excess is *gaussexc*).

E. General Introduction to Individual Coincidence Processing and a One-to-Many Coupling Approach

The calibration process of the time delay for one crystal may include the distinction between all other crystals; one crystal is coincident with. Alternatively, that distinction may be omitted. In the first case, all individual pairs of crystals that were measured have to be handled independently. In the latter case, all measured time differences of a specific crystal can be stored in one single histogram regardless of the coincident crystal.

The first method will result in many time differences measured between unique pairs of coincident crystals and requires either a strategy to solve the overdetermined equation system [26], [27] or to store the calibration values for each combination of crystals. As not all combinations of crystals may be recorded during a calibration, the preferred method would be to find a delay value for each crystal that fits best all the observed time differences.

The one-to-many coupling approach is based on a single time difference distribution per crystal, and the mean time delay can directly be extracted from this distribution. The time difference distribution might be much broader than the optimal CRT the crystal or the system as a whole is able to achieve.

In an uncalibrated system, the individual crystal time delays are initially unknown, which leads to many different time delays contributing to the same time difference spectrum. Therefore, for a one-to-many coupling approach, it is beneficial to iteratively apply the time delay calculation to precisely determine the individual crystal delay values.

F. Sensor Delay Calibration

Sensor delays were calibrated before additional crystal delays or time walk effects were calibrated. As the number of individual sensors with individual TDCs is still rather low (16 per stack), we used an individual sensor coincidence processing scheme. The delays of the sensors in the system were determined using the original method (the same principal as for the crystal delay fit described in Section III-G1) [13]. Once the sensor delays were determined, they were kept constant and only the additional crystal delay values and crystal time walk values were calculated using various combinations of methods described in the following sections.

G. Crystal Delay Calibration

1) Original Method: The original time calibration method, used in the previous publications, is based on an individual coincidence processing scheme and was refined for this paper. It now correctly accounts for the distance of the identified emission source to the crystal. Furthermore, as we accepted only LORs with a maximum distance of 10 mm to the nearest point of emission, we expect fewer wrongly assigned points of emission for the annihilation gammas and thereby a reduced background in the time difference distribution.

The mean time difference and the error on the mean were extracted from the time difference histograms for each of the recorded coincident crystal pairs with at least 100 entries. To all differences, a solution of a single delay value per crystal was fitted using a minimizer. The method had to be simplified (as applied for previously published works) for the *preclinical* configuration using only one delay per crystal position for all stacks to reduce the computational complexity. This means that only 900 crystal delay values, the number of crystals of one stack, were determined for the whole scanner and the same values are used for each of the 60 stacks. In the previously published results of the *preclinical* configuration, we did not determine this delay map for each trigger scheme individually but instead used the same delay calibration obtained with trigger scheme 1 for all other trigger schemes. As we will see in the results, this led to a degradation of the CRT performance reported in the previous publications of the *preclinical* configuration. The described calibration was performed using the reference energy window of 411–561 keV.

2) Iterative One-to-Many Coupling: This method uses the one-to-many coupling approach to determine the crystal individual delay value. The two singles of a coincidence were both checked for the reference energy window, and the time difference is added to both of the crystal time difference histograms. After processing the whole listmode file, the mean of the time difference histogram of each crystal was determined and the delay was added to the delay value obtained in previous iterations. The algorithm was applied iteratively ten times.

H. Time Walk Calibration

We used a time walk model, which linearly depends on the ratio of the photopeak energy to the measured energy of a single [see (1)]. As the photopeak energy of 511 keV was used as a reference, the walk correction was set to zero for a measured energy equal to the photopeak energy

$$T' = T - w_{(i)}\left(\frac{E_{\text{peak}}}{E_{\text{measured}}} - 1\right). \tag{1}$$

Given this definition, $w_{(i)}$ describes the time walk correction for a single with an energy of 256 keV in units of picoseconds. The model in (1) can be applied using a single time walk factor w for the whole system or an individual time walk factor per crystal w_i. For the first case, the optimal value could easily be determined by sweeping the value for w, calculating the CRT for the respective value, and then finding the minimum in the CRT-over-w curve. If an individual value of w_i for each crystal should be determined, this optimization would be too complex and time consuming. Therefore, the crystal individual time walk values w_i had to be determined directly.

TABLE III

TIME CALIBRATION METHODS

abbreviation	description
prev	previously published results
repr	raw data reprocessed with the original method and the changes described in section III-G1
glwalk	global walk model as described in section III-H1 applied to the data obtained with *repr*
inddel	crystal individual delay estimation as described in III-G2
inddel +*glwalk*	an individual delay estimation *inddelay* followed by a global walk estimation (*glwalk*) is iteratively applied
inddel +*indwalk*	an individual delay estimation *inddelay* followed by an individual walk estimation as described in III-H2 is iteratively applied

1) Global Time Walk Calibration by Optimization: As mentioned before, the global time walk factor w could be found via optimization by searching for the value resulting in the best CRT. The best CRT was defined as the minimal FWHM calculated as described in Section III-D. A value for w was chosen, and the complete listmode file was parsed in order to apply the time walk correction in (1) for all coincidences falling into the chosen energy window. This resulted in CRT FWHM values as a function of w as shown in Fig. 8. The minimum was determined by fitting a quadratic function to the minimal data point and the surrounding ±5 data points.

2) Individual Crystal Time Walk Calibration: Crystal individual time walk factors cannot be calculated using the method described in the previous section. Therefore, we used a one-to-many coupling scheme and directly determined the walk factor for each crystal. The energy of the coincident crystal was checked for the reference energy window (411–561 keV) while accepting all energy values for the crystal under calibration. The energy ratio ($E_{\text{peak}}/E_{\text{measured}}$) and the measured time difference corrected for the known source position were filled into a 2-D histogram (see the example in Fig. 9). For each energy ratio bin, the mean delay was computed and a linear regression of the delay value over the energy ratio was performed resulting in the time walk factor w_i. As for the one-to-many coupling approach of the delay calibration (Section III-G2), this method was applied iteratively, which allows to correct for time walk effects of the coincident crystal. The method was applied iteratively ten times.

I. Evaluated Time Delay and Time Walk Calibrations

We evaluated various time delay and time walk calibration methods (described in the previous sections) and combinations of both (see the list with the abbreviations used throughout this paper in Table III). We report up to six CRT values for each measurement and energy window.

IV. RESULTS

The crystal delay maps for the *preclinical* configuration obtained by reapplying the original crystal delay method

(a) *preclinical* configuration, *prev*

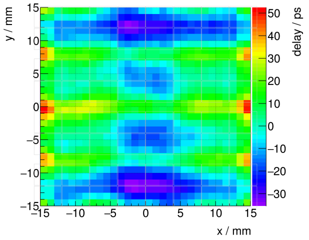

(b) *preclinical* configuration, *repr*, trigger scheme 1

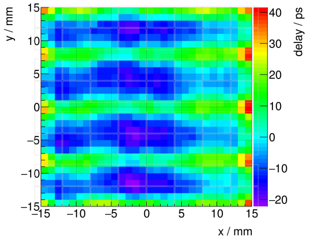

(c) *preclinical* configuration, *repr*, trigger scheme 2

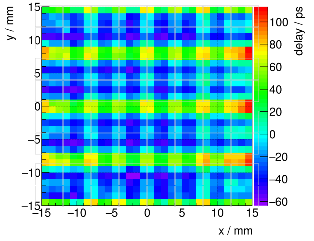

(d) *preclinical* configuration, *repr*, trigger scheme 3

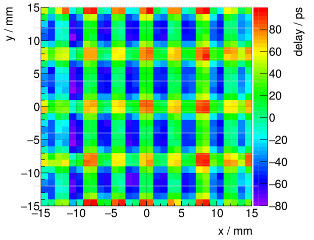

(e) *preclinical* configuration, *repr*, trigger scheme 4

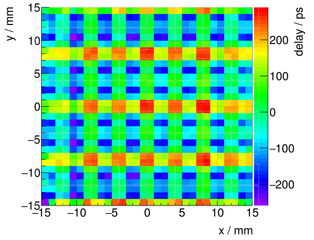

Fig. 7. Crystal delay values for the *preclinical* configuration. The first map shows the original values used for all trigger schemes in the previous publications (reprinted from [13] 🅭🅯3.0). The maps show the crystal delay maps for trigger schemes 1–4 using the original method and having reprocessed the raw data. These maps were applied to all 60 stacks of the *preclinical* configuration. One can clearly see the influence of the position of a crystal. Crystals above bond gaps show a larger delay value, whereas crystals centrally located over a pixel show the lowest delay values. (a) *preclinical* configuration, *prev*. (b) *preclinical* configuration, *repr*, trigger scheme 1. (c) *preclinical* configuration, *repr*, trigger scheme 2. (d) *preclinical* configuration, *repr*, trigger scheme 3. (e) *preclinical* configuration, *repr*, trigger scheme 4.

(*repr*, Section III-G1) are shown in Fig. 7. The previously published map for trigger scheme 1 shows similarities, but is more blurred compared with the one obtained by reprocessing the data (*repr*) [see Fig. 7(a) and (b)], whereas the delay maps for the higher trigger schemes show a higher variability in the delay values between crystal positions. For crystals centrally located above pixels, we determined the lowest delay values in contrast to crystals located above bond gaps, between pixels, and at the edges of the sensor tile for which we determined the highest delay values.

The CRT FWHM as a function of the global walk factor w is reported in Fig. 8. In general, the *preclinical* configuration showed a stronger time walk effect compared with the *clinical* configuration as in the case for larger energy windows and higher trigger schemes. Larger energy windows, for which we determined a stronger time walk effect, tended to show lower optimal time walk factors. When the energy window is confined to a region around the photopeak (500–520 keV), almost no time walk effect can be observed and the CRT reaches the best value for the given set of parameters.

As an example, the first iteration of the crystal individual time walk determination for the *preclinical* configuration using trigger scheme 4 is shown in Fig. 9.

The FWHM results of all conducted calibrations and evaluations are listed for the *preclinical* configuration in Table IV and for the clinical configuration in Table V. FWTM results are reported for the *preclinical* configuration in Table VI and for the *clinical* configuration in Table VII. In Tables IV–VII, the wide energy window (250–625 keV) is marked as it is probably the preferred choice for preclinical studies on the Hyperion II^{D} platform due to the higher sensitivity.

Tables IV–VII also include columns that compare the relative improvement between methods. Reprocessing the raw data with the original method (*repr*) resulted in improvements compared with the previously published results (*prev*) for the wide energy window between 6.9% and 10.9% for the *preclinical* configuration and between 4.4% and 4.8% for the *clinical* configuration depending on the trigger scheme. For the *preclinical* configuration, applying an individual delay calculation together with the global walk determination (*inddel*+*glwalk*) yields an improvement over the reprocessed delay fit method (*repr*) of 0.6%, 2.6%, 1.9%, and 2.7% for trigger schemes 1–4, respectively. The preferred choice of the time correction for the *clinical* configuration is the global walk model (*glwalk*) applied additionally to the reprocessed delay fit method (*repr*), which already determines a crystal individual delay value for this scintillator configuration. Regarding the walk correction, this resulted in an additional improvement by 0.7%, 1.3%, 0.9%, and 1.9% for trigger schemes 1–4, respectively. A similar order of the magnitude of improvements could be observed when looking at the CRT FWTM values.

Interestingly, the improvement of a walk correction was measured to be greater for trigger scheme 2 compared with trigger scheme 3 even though the mean threshold of required SPAD breakdowns is higher in the latter case (2.33±0.67 compared with 3.00 ± 1.40).

Both configurations do not show a large benefit, if any at all, of the individual walk determination compared with

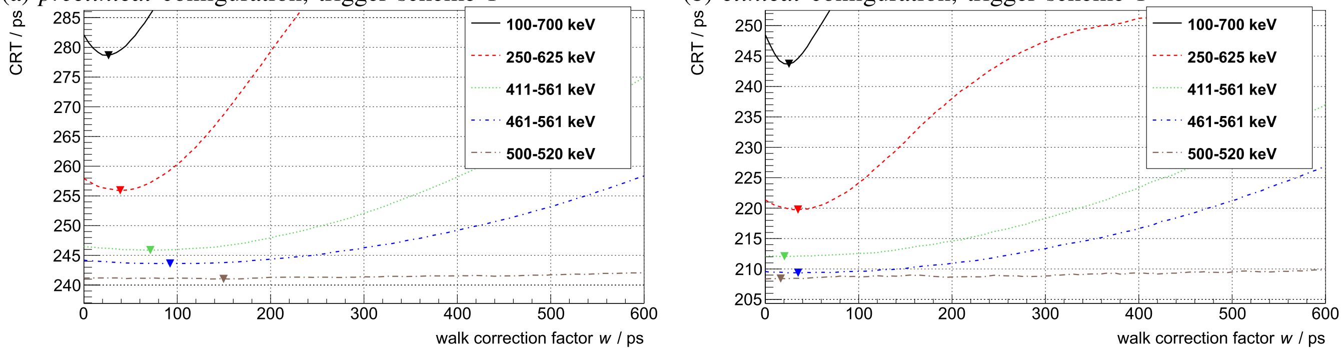
(a) *preclinical* configuration, trigger scheme 1 (b) *clinical* configuration, trigger scheme 1

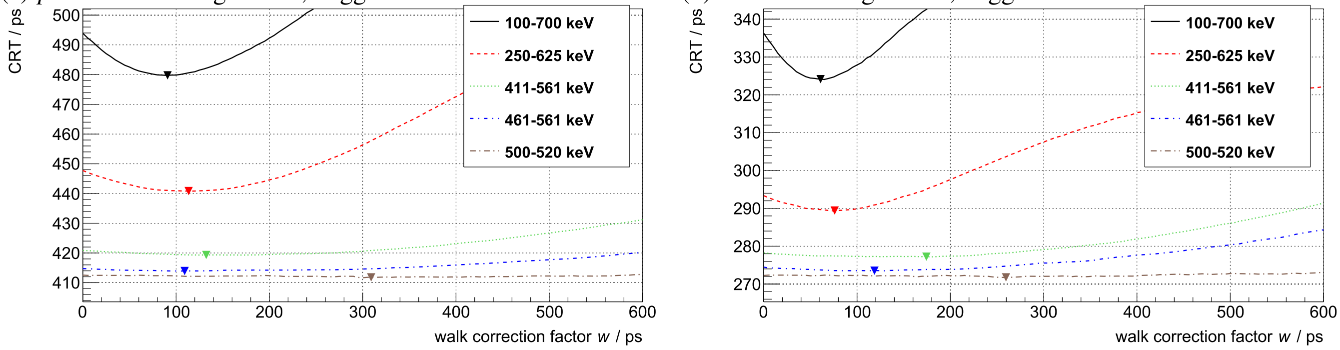
(c) *preclinical* configuration, trigger scheme 2 (d) *clinical* configuration, trigger scheme 2

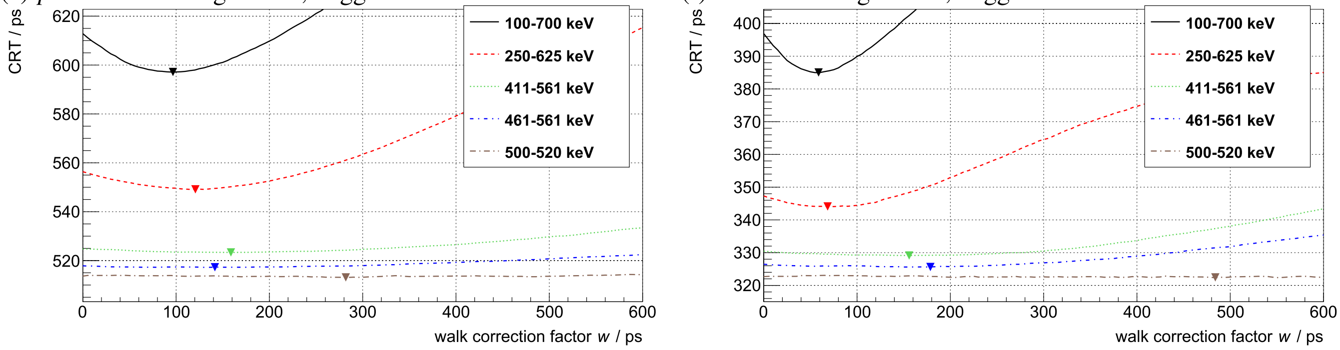
(e) *preclinical* configuration, trigger scheme 3 (f) *clinical* configuration, trigger scheme 3

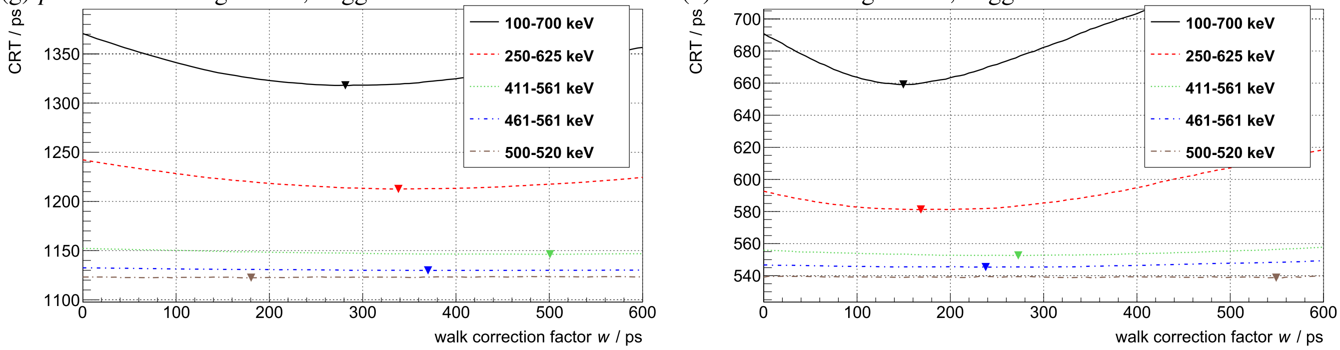
(g) *preclinical* configuration, trigger scheme 4 (h) *clinical* configuration, trigger scheme 4

Fig. 8. Time walk calibration (or optimization) for the model using only a single time walk factor for the whole system. The measurements shown in the left column were conducted using the *preclinical* configuration and the measurements shown in the right column with the *clinical* configuration. Rows from top to bottom show the different trigger schemes from 1 to 4. The different lines show the CRT for different energy windows as a function of the time walk factor w. (a) *Preclinical* configuration, trigger scheme 1. (b) *Clinical* configuration, trigger scheme 1. (c) *Preclinical* configuration, trigger scheme 2. (d) *Clinical* configuration, trigger scheme 2. (e) *Preclinical* configuration, trigger scheme 3. (f) *Clinical* configuration, trigger scheme 3. (g) *Preclinical* configuration, trigger scheme 4. (h) *Clinical* configuration, trigger scheme 4.

the global walk model. Therefore, we marked for the *preclinical* configuration the column reporting the CRT values for the *inddelay+glwalk* method and for the clinical configuration the column reporting the *glwalk* results as we think that these are the methods of choice for the respective configuration.

TABLE IV

CRT FWHM Results for the *Preclinical* Configuration. The Suggested Energy Window (*Wide*, 250–625 keV) and Calibration Method (*Inddel+Glwalk*) Are Marked in Gray. The Last Three Columns Report the Relative Changes From the Previously Published Results to the Reprocessed Results Using the Original Method (*Prev/Repr*), the Previously Published Results to the Method Using Individual Crystal Delays and a Global Walk Model (*Prev/Indel+Glwalk*), and the Reprocessed Results Using the Original Method to the Method Using Individual Crystal Delays and a Global Walk Model (*Repr/Inddel+Glwalk*)

	energy window	*prev*	*repr*	*glwalk*	*inddel*	*inddel +glwalk*	*inddel +indwalk*	*prev /repro*	*prev /inddel+glwalk*	*repr /inddel+glwalk*
		FWHM / ps						improvement		
trig 1	500 keV-520 keV	-	241.2	241.0	240.5	240.4	240.7	-	-	0.3 %
	461 keV-561 keV	-	244.2	243.6	243.3	243.0	243.0	-	-	0.5 %
	411 keV-561 keV	257.6	246.5	245.9	245.6	245.1	245.2	4.3 %	4.8 %	0.6 %
	250 keV-625 keV	282.1	257.9	255.9	257.3	256.4	257.0	8.6 %	9.1 %	0.6 %
	100 keV-700 keV	-	282.1	278.7	281.4	284.1	285.3	-	-	−0.7 %
trig 2	500 keV-520 keV	-	412.6	411.8	404.7	405.2	405.2	-	-	1.8 %
	461 keV-561 keV	-	416.8	415.6	410.1	409.3	408.9	-	-	1.8 %
	411 keV-561 keV	431.9	420.9	419.3	416.1	414.5	414.3	2.5 %	4.0 %	1.5 %
	250 keV-625 keV	481.1	447.7	440.8	443.3	436.1	438.2	6.9 %	9.4 %	2.6 %
	100 keV-700 keV	-	493.9	479.8	489.0	476.5	482.2	-	-	3.5 %
trig 3	500 keV-520 keV	-	513.7	513.1	509.3	509.1	508.6	-	-	0.9 %
	461 keV-561 keV	-	517.9	517.3	513.2	512.6	512.7	-	-	1.0 %
	411 keV-561 keV	537.6	524.7	523.3	520.1	518.7	518.9	2.4 %	3.5 %	1.1 %
	250 keV-625 keV	597.9	556.4	549.2	552.1	545.6	548.9	6.9 %	8.8 %	1.9 %
	100 keV-700 keV	-	612.9	597.2	608.5	595.1	606.2	-	-	2.9 %
trig 4	500 keV-520 keV	-	1123.1	1122.4	1109.9	1110.1	1109.9	-	-	1.2 %
	461 keV-561 keV	-	1132.5	1129.9	1128.9	1126.3	1125.8	-	-	0.5 %
	411 keV-561 keV	1241.3	1152.2	1146.3	1147.1	1141.2	1141.6	7.2 %	8.1 %	1.0 %
	250 keV-625 keV	1394.3	1242.3	1212.7	1237.9	1208.8	1214.0	10.9 %	13.3 %	2.7 %
	100 keV-700 keV	-	1370.6	1318.0	1364.7	1318.7	1336.3	-	-	3.8 %

TABLE V

CRT FWHM Results for the *Clinical* Configuration. The Suggested Energy Window (*Wide*, 250–625 keV) and Calibration Method (*Glwalk*) Are Marked in Gray. The Last Three Columns Report the Relative Changes From the Previously Published Results to the Reprocessed Results Using the Original Method (*Prev/Repr*), the Previously Published Results to the Method Using a Global Walk Model (*Prev/Glwalk*), and the Reprocessed Results Using the Original Method to the Method Using a Global Walk Model (*Repr/Glwalk*)

	energy window	*prev*	*repr*	*glwalk*	*inddel*	*inddel +glwalk*	*inddel +indwalk*	*prev /repr*	*prev /glwalk*	*repr /glwalk*
		FWHM / ps						improvement		
trig 1	500 keV-520 keV	-	208.4	208.4	208.9	208.9	209.0	-	-	0.0 %
	461 keV-561 keV	215.2	209.6	209.4	209.6	209.5	209.6	2.6 %	2.7 %	0.1 %
	411 keV-561 keV	-	212.1	212.1	212.3	212.1	212.4	-	-	0.0 %
	250 keV-625 keV	232.4	221.4	219.8	221.4	219.9	222.6	4.8 %	5.4 %	0.7 %
	100 keV-700 keV	-	248.5	243.7	248.7	244.7	256.5	-	-	1.9 %
trig 2	500 keV-520 keV	-	272.3	271.8	272.4	272.5	272.6	-	-	0.2 %
	461 keV-561 keV	279.1	274.5	273.5	274.3	273.6	273.6	1.7 %	2.0 %	0.3 %
	411 keV-561 keV	-	278.2	277.2	278.1	277.2	277.2	-	-	0.4 %
	250 keV-625 keV	307.3	293.4	289.4	293.3	291.2	292.6	4.5 %	5.8 %	1.3 %
	100 keV-700 keV	-	336.3	324.2	336.2	332.0	337.3	-	-	3.6 %
trig 3	500 keV-520 keV	-	322.7	322.5	323.3	323.2	323.3	-	-	0.1 %
	461 keV-561 keV	332.7	326.5	325.6	326.4	325.8	325.9	1.9 %	2.1 %	0.3 %
	411 keV-561 keV	-	330.5	329.1	330.5	329.1	329.2	-	-	0.4 %
	250 keV-625 keV	363.4	347.3	344.1	347.1	347.6	349.6	4.4 %	5.3 %	0.9 %
	100 keV-700 keV	-	396.9	385.0	396.9	400.7	405.8	-	-	3.0 %
trig 4	500 keV-520 keV	-	539.1	538.8	540.5	540.5	540.1	-	-	0.1 %
	461 keV-561 keV	557.0	546.7	545.4	547.7	546.2	546.7	1.9 %	2.1 %	0.2 %
	411 keV-561 keV	-	555.8	552.6	556.4	553.2	554.1	-	-	0.6 %
	250 keV-625 keV	621.1	592.7	581.3	593.0	583.4	592.2	4.6 %	6.4 %	1.9 %
	100 keV-700 keV	-	690.9	659.2	691.4	673.1	696.9	-	-	4.6 %

Fig. 10 shows the time difference distribution for the *preclinical* configuration using trigger scheme 4 and the wide energy window for both the reprocessed data using the original method (*repr*) and, for comparison, the time difference distribution of the method determining individual delay values per crystal and using a global walk model (*inddel+glwalk*).

TABLE VI

CRT FWTM AND GAUSSIAN EXCESS (*Gaussexc*) RESULTS FOR THE *Preclinical* CONFIGURATION. THE SUGGESTED ENERGY WINDOW (*Wide*, 250–625 keV) AND CALIBRATION METHOD (*Inddel+Glwalk*) ARE MARKED IN GRAY. THE LAST COLUMN REPORTS THE RELATIVE CHANGE FROM THE REPROCESSED DATA USING THE ORIGINAL METHOD TO THE METHOD USING INDIVIDUAL CRYSTAL DELAY VALUES AND A GLOBAL WALK MODEL (*Repr/Inddel+Glwalk*)

		repr		*glwalk*		*inddel*		*inddel+glwalk*		*inddel+indwalk*		*repr /inddel+glwalk*
	energy window	FWTM / ps	gaussexc	FWTM / ps	gaussexc	FWTM / ps	gaussexc	FWTM / ps	gaussexc	FWTM / ps	gaussexc	improvement
trig 1	500 keV-520 keV	479.7	9.1 %	479.7	9.2 %	476.6	8.7 %	476.4	8.7 %	476.6	8.6 %	0.7 %
	461 keV-561 keV	485.6	9.1 %	484.8	9.1 %	482.5	8.8 %	481.8	8.8 %	481.8	8.7 %	0.8 %
	411 keV-561 keV	491.5	9.3 %	490.2	9.3 %	488.4	9.1 %	487.1	9.0 %	478.1	7.0 %	0.9 %
	250 keV-625 keV	526.6	12.0 %	519.8	11.4 %	524.2	11.7 %	516.6	10.5 %	517.4	10.4 %	1.9 %
	100 keV-700 keV	654.4	27.2 %	620.9	22.2 %	651.8	27.0 %	615.6	18.9 %	623.8	19.9 %	5.9 %
trig 2	500 keV-520 keV	804.8	7.0 %	804.6	7.2 %	793.9	7.6 %	794.2	7.5 %	794.2	7.5 %	1.3 %
	461 keV-561 keV	819.0	7.8 %	816.4	7.7 %	802.6	7.3 %	800.7	7.3 %	800.2	7.3 %	2.2 %
	411 keV-561 keV	827.9	7.9 %	823.9	7.8 %	816.4	7.6 %	812.5	7.5 %	811.7	7.5 %	1.9 %
	250 keV-625 keV	906.7	11.1 %	881.2	9.6 %	896.6	10.9 %	870.3	9.4 %	870.5	8.9 %	4.0 %
	100 keV-700 keV	1184.8	31.6 %	1056.1	20.7 %	1172.3	31.5 %	1033.1	18.9 %	1051.0	19.6 %	12.8 %
trig 3	500 keV-520 keV	1032.4	10.2 %	1032.2	10.3 %	1021.2	10.0 %	1020.8	10.0 %	1020.5	10.1 %	1.1 %
	461 keV-561 keV	1044.0	10.6 %	1042.5	10.5 %	1032.1	10.3 %	1030.3	10.2 %	1029.7	10.2 %	1.3 %
	411 keV-561 keV	1060.3	10.8 %	1056.4	10.7 %	1047.6	10.5 %	1044.1	10.4 %	1043.3	10.3 %	1.5 %
	250 keV-625 keV	1153.4	13.7 %	1127.4	12.6 %	1141.2	13.4 %	1115.3	12.1 %	1115.8	11.5 %	3.3 %
	100 keV-700 keV	1486.9	33.1 %	1352.8	24.2 %	1469.8	32.5 %	1320.9	21.7 %	1344.1	21.6 %	11.2 %
trig 4	500 keV-520 keV	2323.2	13.4 %	2323.2	13.5 %	2278.7	12.6 %	2279.9	12.6 %	2280.1	12.7 %	1.9 %
	461 keV-561 keV	2359.6	14.3 %	2353.0	14.2 %	2317.9	12.6 %	2311.0	12.5 %	2309.6	12.5 %	2.1 %
	411 keV-561 keV	2407.3	14.6 %	2391.3	14.4 %	2362.5	13.0 %	2348.8	12.9 %	2346.8	12.7 %	2.4 %
	250 keV-625 keV	2692.8	18.9 %	2594.4	17.3 %	2646.6	17.3 %	2541.9	15.3 %	2537.2	14.6 %	5.6 %
	100 keV-700 keV	3578.7	43.2 %	3153.9	31.2 %	3508.2	41.0 %	3014.4	25.4 %	2990.2	22.7 %	15.8 %

TABLE VII

CRT FWTM AND GAUSSIAN EXCESS (*Gaussexc*) RESULTS FOR THE *Clinical* CONFIGURATION. THE SUGGESTED ENERGY WINDOW (*Wide*, 250–625 keV) AND CALIBRATION METHOD (*Glwalk*) ARE MARKED IN GRAY. THE LAST COLUMN REPORTS THE RELATIVE CHANGE FROM THE REPROCESSED DATA USING THE ORIGINAL METHOD TO THE METHOD USING A GLOBAL WALK MODEL (*Repr/Glwalk*)

		repr		*glwalk*		*inddel*		*inddel+glwalk*		*inddel+indwalk*		*repr /glwalk*
	energy window	FWTM / ps	gaussexc	FWTM / ps	gaussexc	FWTM / ps	gaussexc	FWTM / ps	gaussexc	FWTM / ps	gaussexc	improvement
trig 1	500 keV-520 keV	413.0	8.7 %	412.9	8.7 %	412.9	8.4 %	413.0	8.4 %	412.9	8.4 %	0.0 %
	461 keV-561 keV	416.7	9.0 %	416.3	9.1 %	416.8	9.1 %	416.3	9.0 %	416.3	8.9 %	0.1 %
	411 keV-561 keV	422.8	9.3 %	422.4	9.2 %	422.8	9.2 %	422.1	9.1 %	421.9	9.0 %	0.1 %
	250 keV-625 keV	454.0	12.5 %	447.3	11.6 %	453.9	12.4 %	447.1	11.5 %	447.2	10.2 %	1.5 %
	100 keV-700 keV	605.2	33.6 %	560.2	26.1 %	605.2	33.5 %	551.3	23.6 %	577.7	23.5 %	7.4 %
trig 2	500 keV-520 keV	539.5	8.7 %	539.8	8.9 %	539.2	8.6 %	539.6	8.6 %	539.7	8.6 %	−0.1 %
	461 keV-561 keV	546.3	9.2 %	544.7	9.2 %	546.2	9.2 %	544.6	9.2 %	544.5	9.1 %	0.3 %
	411 keV-561 keV	555.7	9.5 %	551.6	9.1 %	555.7	9.6 %	552.2	9.2 %	551.8	9.2 %	0.7 %
	250 keV-625 keV	607.8	13.6 %	590.5	11.9 %	607.7	13.6 %	588.6	10.9 %	590.5	10.7 %	2.8 %
	100 keV-700 keV	904.9	47.6 %	768.8	30.1 %	904.9	47.6 %	764.9	26.4 %	791.0	28.6 %	15.0 %
trig 3	500 keV-520 keV	664.3	12.9 %	665.0	13.1 %	664.5	12.7 %	664.7	12.8 %	664.8	12.8 %	−0.1 %
	461 keV-561 keV	673.4	13.1 %	672.1	13.2 %	673.4	13.2 %	672.0	13.1 %	672.0	13.1 %	0.2 %
	411 keV-561 keV	684.3	13.6 %	681.0	13.5 %	684.3	13.6 %	680.9	13.5 %	680.8	13.4 %	0.5 %
	250 keV-625 keV	743.8	17.5 %	728.8	16.2 %	743.7	17.5 %	726.0	14.6 %	728.0	14.2 %	2.0 %
	100 keV-700 keV	1080.5	49.3 %	952.8	35.7 %	1080.4	49.3 %	952.2	30.3 %	977.3	32.1 %	11.8 %
trig 4	500 keV-520 keV	1161.9	18.2 %	1163.9	18.5 %	1163.2	18.0 %	1162.8	18.0 %	1163.1	18.1 %	−0.2 %
	461 keV-561 keV	1182.8	18.7 %	1179.6	18.6 %	1183.1	18.5 %	1179.4	18.4 %	1179.5	18.3 %	0.3 %
	411 keV-561 keV	1207.0	19.1 %	1199.3	19.0 %	1207.1	19.0 %	1199.8	19.0 %	1198.8	18.7 %	0.6 %
	250 keV-625 keV	1341.8	24.2 %	1270.0	19.8 %	1341.8	24.1 %	1289.2	21.2 %	1294.6	19.9 %	5.4 %
	100 keV-700 keV	2164.7	71.9 %	1782.0	48.3 %	2163.9	71.7 %	1714.1	39.7 %	1798.2	41.5 %	17.7 %

This is the set of parameters that show the biggest improvement (2.7%) for the *preclinical* configuration using the preferred parameters and time calibration method.

As an example for a small improvement (0.7%), Fig. 11 shows the time difference distribution for the *clinical* configuration using trigger scheme 1 and the wide energy window for both the reprocessed data using the original method (*repr*) and, for comparison, the time difference distribution of the method using a global walk model (*glwalk*).

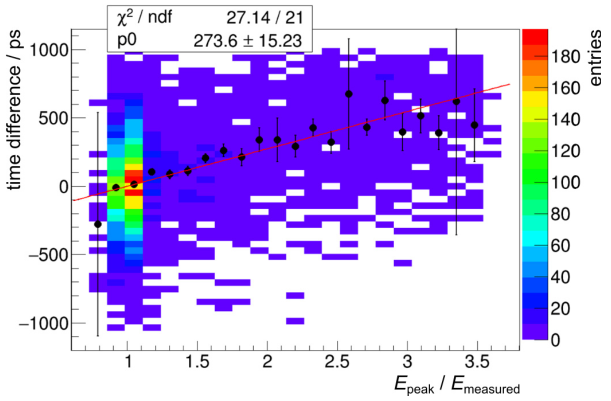

Fig. 9. Time walk calibration for a single selected crystal. The measurement was conducted using the *clinical* configuration and trigger scheme 4.

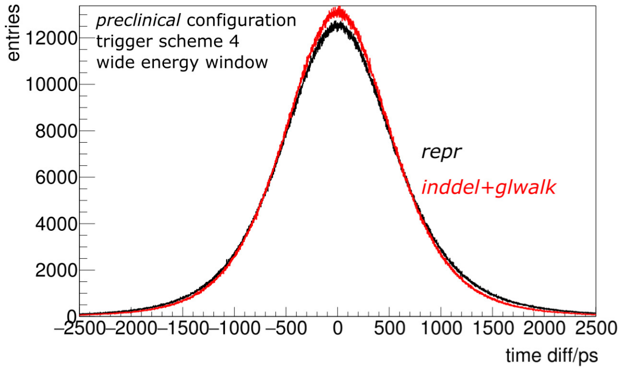

Fig. 10. Time difference histograms for the *preclinical* configuration using trigger scheme 4 and the wide energy window. In black, the time difference distribution for the original method is shown (*repr*), which uses the same time delay map [see Fig. 7(e)] for all of the 60 detector stacks. The time difference distribution for the method determining individual delay values per crystal and using a global walk model (*inddel+glwalk*) is shown in red.

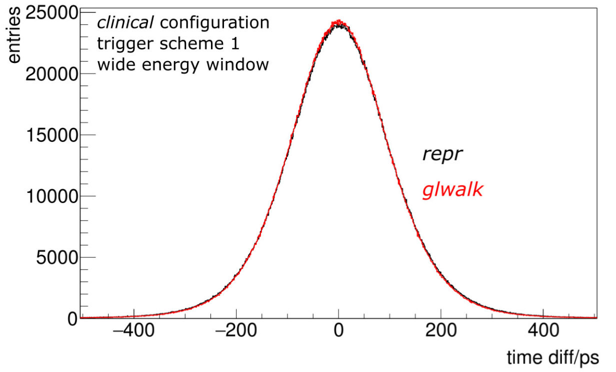

Fig. 11. Time difference histograms for the *clinical* configuration using trigger scheme 1 and the wide energy window. In black, the time difference distribution for the original method is shown (*repr*) and in red the time difference distribution additionally using a global walk model (*glwalk*).

V. CONCLUSION

The different delay patterns for the trigger schemes shown in Fig. 7 are caused in case of trigger scheme 1 by the location of light-sensitive SPADs and light-insensitive areas like the bond gaps between rows of DPCs (the bond gaps are sketched in Fig. 2). The higher trigger schemes showed an additional pattern caused by the logical combinations of subpixel trigger lines in order to generate the global trigger signal. For example, trigger scheme 3 requires that one photon is detected both on the two left subpixels and the two right subpixels. Therefore, vertical lines of high delay values in the delay maps can be identified, as these crystals only illuminate one of the two required trigger regions efficiently. Nonetheless, all higher trigger schemes showed the lowest delay for crystals located centrally above a pixel because these crystal positions allow illuminating the four subpixels homogeneously.

The stronger decline of the *preclinical* configuration in CRT performance when going to higher trigger settings compared with the *clinical* configuration can be explained by the different photon densities on the photosensors. The *clinical* configuration focuses all scintillation photons on a single pixel of the DPC and therefore optimally illuminates all required subpixels even for the higher trigger settings. The light guide used in the *preclinical* configuration leads to a much broader light pattern on the sensor tile and therefore also a lower photon density, especially on the subpixels that are not located directly beneath the scintillating crystal.

A higher improvement in CRT when applying a walk correction was observed for trigger scheme 2 compared with trigger scheme 3. This is due to the fact that trigger scheme 2 has a narrower probability distribution for the amount of detected SPAD breakdowns needed to generate the trigger signal (2.33 ± 0.67 compared with 3.00 ± 1.40) (see Table I and [23]). Thus, the jitter introduced by the threshold itself is smaller.

A digital trigger handling allowing us to trigger on the *n*th SPAD breakdown rather than combining larger trigger regions, as does the used DPC with subpixels, would thus probably allow achieving better timing resolutions, and would show a higher improvement when applying a walk correction, as one could get rid of the additional jitter introduced by the trigger threshold's probability distribution.

In conclusion, we could improve the CRT performance of the Hyperion II^D platform compared with previously reported results. This was mainly achieved by optimizing the already published method of fitting a delay value for each crystal. We will discuss the wide energy window together with trigger scheme 2 here, as this setting offers a very good timing performance and still results in a good sensitivity of the system. Compared with previously published results, we could improve the timing performance of our PET system by only applying a delay correction for this set of parameters by 7.8% for the *preclinical* and by 4.5% for the *clinical* configuration in terms of FWHM (we did not publish FWTM results before). Adding a walk correction helped to improve the CRT by 2.6% (1.3%) in terms of FWHM and 4.0% (2.8%) in terms of FWTM for the *preclinical* (*clinical*) configuration. To the best of our knowledge, the CRT FWHM of 436.1 ps for the *preclinical* configuration and 289.4 ps for the *clinical* configuration are among the best CRT values for a PET system operated under normal imaging-capable conditions shown so far. Using trigger scheme 1 and the photopeak energy range of 500–520 keV results in the best CRT we were able to measure with the system, which was 240.4 ps for the *preclinical* configuration and 208.4 ps for the *clinical* configuration. This combination of trigger scheme 1 and the very narrow photopeak energy range is not a setting of parameters one would choose for imaging applications, but merely a setting to measure CRT record values.

For a single-sided-readout setup of a monolithic scintillator with a length of 22 mm read out by the same DPC sensors, CRT values of 214 ps were reported [28] (For a dual-sided readout scheme, the same group achieved a CRT of 147 ps FWHM [29]). In that experiment, the operating temperature was set to −25 °C and the employed energy window was reported as FWTM, which translates (with the reported energy resolution of 9.9% FWHM) to 465–565 keV and thus should roughly correspond to the values reported in this paper for the *photopeak wide* energy range of 461–561 keV. Those results exceed the values reported in this paper and demonstrate what can be achieved in bench-top experiments with sophisticated positioning and time stamp algorithms using a single detector block, trigger scheme 1, and very low temperatures. According to our research, trigger setting 1 is challenging to implement on system level at higher sensor temperatures without loosing sensitivity [5]. Another group evaluated thin monolithic detectors (2- and 5-mm thickness) coupled to DPCs in bench top experiments using trigger setting 2 and sensor temperatures of 3 °C–6 °C. That group achieved a CRT of 680 ps FWHM with a first setup [30] and could improve it to 529 ps FWHM in a second experiment [31]. Those results might indicate that even thin monolithic detectors show a decline in CRT performance when higher trigger settings are used. Most likely, that decline can be attributed to the low photon density, discussed at the beginning of this section, which is expected to be even lower than the photon density of the *preclinical* configuration presented in this paper.

The clinical PET scanner with the best timing performance reported is the Philips Vereos PET/CT [32], which uses the same DPC sensors as the Hyperion II^D platform with 22-mm-long crystals, and for which a CRT of 307–316 ps was measured [10], [33].

As the individual walk determination is much more prone to limitations in the available statistics and the prevention of calibration artifacts for individual crystals is not trivial, we conclude that the global walk model is much more robust and should be the preferred choice. We conclude that a stable and precise determination of the time delays for each crystal is of importance, but the additional gain of adding a time walk correction is rather small. The object scatter in the investigated activity distribution is rather low and as a result the fraction of singles with a high energy still quite high. When more object scatter is to be expected, the time walk correction might gain importance as low-energy gammas will occur more often.

To further improve the CRT, we could use higher overvoltages and reduce the inhibit fraction. Both values ($V_{\text{OV}} = 2.5$ V and an inhibit fraction of 20%) are chosen conservatively, and previous measurements suggest that more aggressive settings lead to an improvement of the CRT [5].

With the ability to store raw DPC data, the Hyperion II^D platform is an interesting PET platform for research applications, as it enables the exploration of sophisticated data processing steps. It provides very competitive CRT values (which could be further improved in this paper) and is able to maintain this performance when operated simultaneously in an MRI scanner [6].

VI. ACKNOWLEDGMENT

The authors would like to thank T. Solf and T. Frach from Philips Digital Photon Counting for many fruitful discussions regarding timing calibration.

REFERENCES

[1] B. Weissler *et al.*, "A digital preclinical PET/MRI insert and initial results," *IEEE Trans. Med. Imag.*, vol. 34, no. 11, pp. 2258–2270, Nov. 2015, doi: 10.1109/TMI.2015.2427993.

[2] J. Wehner *et al.*, "MR-compatibility assessment of the first preclinical PET-MRI insert equipped with digital silicon photomultipliers," *Phys. Med. Biol.*, vol. 60, no. 6, p. 2231, 2015, doi: 10.1088/0031-9155/60/6/2231.

[3] J. Wehner *et al.*, "PET/MRI insert using digital SiPMs: Investigation of MR-compatibility," *Nucl. Instrum. Methods Phys. Res. A, Accel. Spectrom. Detect. Assoc. Equip.*, vol. 734, pp. 116–121, Jan. 2014, doi: 10.1016/j.nima.2013.08.077.

[4] D. R. Schaart, E. Charbon, T. Frach, and V. Schulz, "Advances in digital SiPMs and their application in biomedical imaging," *Nucl. Instrum. Methods Phys. Res. A, Accel. Spectrom. Detect. Assoc. Equip.*, vol. 809, pp. 31–52, Feb. 2016, doi: 10.1016/j.nima.2015.10.078.

[5] D. Schug *et al.*, "Initial PET performance evaluation of a preclinical insert for PET/MRI with digital SiPM technology," *Phys. Med. Biol.*, vol. 61, no. 7, p. 2851, 2016, doi: 10.1088/0031-9155/61/7/2851.

[6] D. Schug *et al.*, "PET performance and MRI compatibility evaluation of a digital, ToF-capable PET/MRI insert equipped with clinical scintillators," *Phys. Med. Biol.*, vol. 60, no. 18, p. 7045, 2015, doi: 10.1088/0031-9155/60/18/7045.

[7] D. L. Bailey, *Positron Emission Tomography: Basic Sciences*. London, U.K.: Springer-Verlag, 2005.

[8] M. Conti, "Focus on time-of-flight PET: The benefits of improved time resolution," *Eur. J. Nucl. Med. Molecular Imag.*, vol. 38, no. 6, pp. 1147–1157, 2011, doi: 10.1007/s00259-010-1711-y.

[9] M. E. Phelps, Ed., *PET: Physics, Instrumentation, and Scanners*. New York, NY, USA: Springer, 2006.

[10] M. Miller *et al.*, "Characterization of the vereos digital photon counting PET system," *J. Nucl. Med.*, vol. 56, no. 3, p. 434, 2015.

[11] B. Goldschmidt *et al.*, "Software-based real-time acquisition and processing of PET detector raw data," *IEEE Trans. Biomed. Eng.*, vol. 63, no. 2, pp. 316–327, Feb. 2016, doi: 10.1109/TBME.2015.2456640.

[12] G. F. Knoll, *Radiation Detection and Measurement*. Hoboken, NJ, USA: Wiley, 2010.

[13] D. Schug *et al.*, "Data processing for a high resolution preclinical PET detector based on philips DPC digital SiPMs," *IEEE Trans. Nucl. Sci.*, vol. 62, no. 3, pp. 669–678, Jun. 2015, doi: 10.1109/TNS.2015.2420578.

[14] T. Frach, G. Prescher, C. Degenhardt, R. de Gruyter, A. Schmitz, and R. Ballizany, "The digital silicon photomultiplier—Principle of operation and intrinsic detector performance," in *Proc. IEEE Nucl. Sci. Symp. Conf. Rec. (NSS/MIC)*, Oct./Nov. 2009, pp. 1959–1965, doi: 10.1109/NSSMIC.2009.5402143.

[15] C. Degenhardt *et al.*, "The digital silicon photomultiplier—A novel sensor for the detection of scintillation light," in *Proc. IEEE Nucl. Sci. Symp. Conf. Rec. (NSS/MIC)*, Oct./Nov. 2009, pp. 2383–2386, doi: 10.1109/NSSMIC.2009.5402190.

[16] T. Frach, G. Prescher, C. Degenhardt, and B. Zwaans, "The digital silicon photomultiplier—System architecture and performance evaluation," in *Proc. IEEE Nucl. Sci. Symp. Conf. Rec. (NSS/MIC)*, Oct./Nov. 2010, pp. 1722–1727, doi: 10.1109/NSSMIC.2010.5874069.

[17] C. Degenhardt, B. Zwaans, T. Frach, and R. de Gruyter, "Arrays of digital silicon photomultipliers—Intrinsic performance and application to scintillator readout," in *Proc. IEEE Nucl. Sci. Symp. Conf. Rec. (NSS/MIC)*, Oct./Nov. 2010, pp. 1954–1956, doi: 10.1109/NSSMIC.2010.5874115.

[18] P. M. Düppenbecker *et al.*, "Development of an MRI-compatible digital SiPM detector stack for simultaneous PET/MRI," *Biomed. Phys. Eng. Exp.*, vol. 2, no. 1, p. 015010, 2016, doi: 10.1088/2057-1976/2/1/015010.

[19] B. Weissler, P. Gebhardt, M. Zinke, F. Kiessling, and V. Schulz, "An MR-compatible singles detection and processing unit for simultaneous preclinical PET/MR," in *Proc. IEEE Nucl. Sci. Symp. Med. Imag. Conf. (NSS/MIC)*, Oct. 2012, pp. 2759–2761, doi: 10.1109/NSSMIC.2012.6551628.

[20] B. Goldschmidt, C. W. Lerche, T. Solf, A. Salomon, F. Kiessling, and V. Schulz, "Towards software-based real-time singles and coincidence processing of digital PET detector raw data," *IEEE Trans. Nucl. Sci.*, vol. 60, no. 3, pp. 1550–1559, Jun. 2013, doi: 10.1109/TNS.2013.2252193.

[21] D. Schug *et al.*, "ToF performance evaluation of PET modules with digital silicon photomultiplier technology during MR operation," *IEEE Trans. Nucl. Sci.*, vol. 62, no. 3, pp. 658–663, Jun. 2015, doi: 10.1109/TNS.2015.2396295.

[22] B. Weissler *et al.*, "Design concept of world's first preclinical PET/MR insert with fully digital silicon photomultiplier technology," in *Proc. IEEE Nucl. Sci. Symp. Med. Imag. Conf. (NSS/MIC)*, Oct./Nov. 2012, pp. 2113–2116, doi: 10.1109/NSSMIC.2012.6551484.

[23] V. Tabacchini, V. Westerwoudt, G. Borghi, S. Seifert, and D. R. Schaart, "Probabilities of triggering and validation in a digital silicon photomultiplier," *J. Instrum.*, vol. 9, no. 6, p. P06016, 2014, doi: 10.1088/1748-0221/9/06/P06016.

[24] S. E. Brunner, L. Gruber, A. Hirtl, K. Suzuki, J. Marton, and D. R. Schaart, "A comprehensive characterization of the time resolution of the philips digital photon counter," *J. Instrum.*, vol. 11, no. 11, p. P11004, 2016, doi: 10.1088/1748-0221/11/11/P11004.

[25] *TILE-TEK USER MANUAL V0.33*, Philips Digit. Photon Counting, Aachen, Germany, 2015.

[26] A. B. Mann, S. Paul, A. Tapfer, V. C. Spanoudaki, and S. I. Ziegler, "A computing efficient PET time calibration method based on pseudoinverse matrices," in *Proc. IEEE Nucl. Sci. Symp. Conf. Rec. (NSS/MIC)*, Oct./Nov. 2009, pp. 3889–3892, doi: 10.1109/NSSMIC.2009.5401925.

[27] P. D. Reynolds, P. D. Olcott, G. Pratx, F. W. Y. Lau, and C. S. Levin, "Convex optimization of coincidence time resolution for a high-resolution PET system," *IEEE Trans. Med. Imag.*, vol. 30, no. 2, pp. 391–400, Feb. 2011, doi: 10.1109/TMI.2010.2080282.

[28] G. Borghi, V. Tabacchini, and D. R. Schaart, "Towards monolithic scintillator based TOF-PET systems: Practical methods for detector calibration and operation," *Phys. Med. Biol.*, vol. 61, no. 13, pp. 4904–4928, 2016, doi: 10.1088/0031-9155/61/13/4904.

[29] G. Borghi, B. J. Peet, V. Tabacchini, and D. R. Schaart, "A 32 mm × 32 mm × 22 mm monolithic LYSO:Ce detector with dual-sided digital photon counter readout for ultrahigh-performance TOF-PET and TOF-PET/MRI.," *Phys. Med. Biol.*, vol. 61, no. 13, pp. 4929–4949, 2016, doi: 10.1088/0031-9155/61/13/4929.

[30] S. España, R. Marcinkowski, V. Keereman, S. Vandenberghe, and R. Van Holen, "DigiPET: Sub-millimeter spatial resolution small-animal PET imaging using thin monolithic scintillators," *Phys. Med. Biol.*, vol. 59, no. 13, p. 3405, 2014, doi: 10.1088/0031-9155/59/13/3405.

[31] R. Marcinkowski, P. Mollet, R. Van Holen, and S. Vandenberghe, "Sub-millimetre DOI detector based on monolithic LYSO and digital SiPM for a dedicated small-animal PET system," *Phys. Med. Biol.*, vol. 61, no. 5, p. 2196, 2016, doi: 10.1088/0031-9155/61/5/2196.

[32] S. Surti and J. S. Karp, "Advances in time-of-flight PET," *Phys. Med.*, vol. 32, no. 1, pp. 12–22, 2016, doi: 10.1016/j.ejmp.2015.12.007.

[33] M. Miller *et al.*, "Initial characterization of a prototype digital photon counting PET system," *J. Nucl. Med.*, vol. 55, no. 1, p. 658, 2014.